

RESEARCH ARTICLE | APRIL 17 2024

Intermittency, bursty turbulence, and ion and electron phase-space holes formation in collisionless current-carrying plasmas

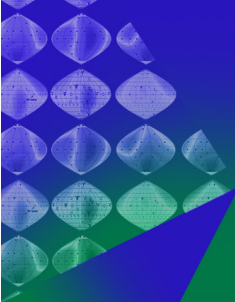
Jian Chen ; Alexander V. Khrabrov ; Igor D. Kaganovich ; He-Ping Li 



Phys. Plasmas 31, 042112 (2024)

<https://doi.org/10.1063/5.0197955>





Physics of Plasmas

Features in Plasma Physics Webinars

Register Today!



Intermittency, bursty turbulence, and ion and electron phase-space holes formation in collisionless current-carrying plasmas

Cite as: Phys. Plasmas **31**, 042112 (2024); doi: 10.1063/5.0197955

Submitted: 15 January 2024 · Accepted: 27 March 2024 ·

Published Online: 17 April 2024



View Online



Export Citation



CrossMark

Jian Chen,^{1,2,a)} Alexander V. Khrabrov,³ Igor D. Kaganovich,^{3,a)} and He-Ping Li^{2,a)}

AFFILIATIONS

¹Sino-French Institute of Nuclear Engineering and Technology, Sun Yat-sen University, Zhuhai 519082, People's Republic of China

²Department of Engineering Physics, Tsinghua University, Beijing 100084, People's Republic of China

³Princeton Plasma Physics Laboratory, Princeton, New Jersey 08543, USA

^{a)}Authors to whom correspondence should be addressed: chenjian5@mail.sysu.edu.cn; ikaganov@pppl.gov; and liheping@mail.tsinghua.edu.cn

ABSTRACT

In the previous studies of nonlinear saturation of the Buneman instability caused by high electron drift velocity relative to ions, the phase-space holes and the plateau on the electron velocity distribution function were identified as features of the saturation stage of instability [notably in the paper by Omura *et al.*, J. Geophys. Res. **108**, 1197 (2003)]. We have performed a much longer simulation of the Buneman instability and observed a secondary instability. This secondary instability generates fast electron-acoustic waves. By analyzing the phase-space plot of ions and electrons, we show that the fast electron heating and the formation of the plateau of electron velocity distribution function are not due to the quasi-linear diffusion but due to the nonlinear interaction of ion- and electron-acoustic solitary waves (phase-space holes) by exchange of trapped electrons in each wave. We also report the details on the intermittent and bursty nature of turbulence driven by this instability.

© 2024 Author(s). All article content, except where otherwise noted, is licensed under a Creative Commons Attribution (CC BY) license (<https://creativecommons.org/licenses/by/4.0/>). <https://doi.org/10.1063/5.0197955>

I. INTRODUCTION

We revisit the evolution of turbulence in current-carrying plasmas by performing long-term particle-in-cell (PIC) simulations to identify complex nonlinear processes that determine the turbulence properties. Current-carrying collisionless plasmas exhibit excitation of a multitude of nonlinear waves and complex turbulence. When the relative drift velocity between the electrons and ions, v_D , exceeds a critical value, the current-driven instability develops in such a system; in particular, the instability is strongest when v_D exceeds the electron thermal velocity, v_{Te} .¹ The instability reaches a nonlinear level and transforms into turbulence that is responsible for several important transport phenomena including anomalous resistivity and electron heating,^{1–4} both of which have been observed in plasmas used in a range of applications, including the tokamak startup,^{5,6} hollow cathode discharges,^{2–4,7,8} space plasmas,^{9–13} etc. Extensive efforts have been devoted to better understanding the correlation between the abrupt change of the macroscopic parameters (i.e., the electron temperature) and the underlying microscopic turbulence physics. However, many effects have still been not well studied and understood.

Understanding the coupling effects between the ion and electron waves and their influence on phase-space hole formation and anomalous electron heating is the motivation for this study. In warm current-carrying plasmas, ion-acoustic waves (IAWs) are generated during the onset of the Buneman instability.¹⁴ Nonlinear processes such as the formation of double layers and phase-space holes were also identified.^{15–20} In addition to that, fast and high-frequency electron waves are also observed both in simulations and experiments.^{9–11,21–23} Specifically, the analysis of the cluster mission data identified electron holes propagating in the Earth's magnetotail, which are likely generated by the Buneman instability and responsible for electron and ion heating.⁹ Kinetic simulations by Che *et al.*¹¹ have further proven that in a current sheet, the Buneman instability grows and traps some electrons while the remaining energetic electrons can drive a two-stream instability. A similar phenomenon of the closely coupled Buneman instability and electron two-stream instability were also observed in plasma devices utilized in electric propulsion and are responsible for the anomalous electron transport in the thrusters' plume regions.^{7,23}

Recently, millisecond measurements of the electron particle fluxes were performed on the magnetospheric multiscale (MMS) mission satellites. The agreement between the measured electron fluxes and the predictions of the 1D model of electron phase-space holes proves the existence of multiple electron phase-space holes in the magnetopause reconnection region.^{10,24} In their measurements, spiky electric field profiles were observed to occasionally appear in a bursty manner, implying intermittent turbulence. Despite the direct evidence provided by the measurements, the physics associated with the intermittency and phase-space hole formation is not very clear and requires precise modeling, which is the main motivation of our study.

So far, many kinetic simulations of current-carrying plasmas have been performed.^{5,11,20–23} Specifically, Omura *et al.*²⁵ studied the nonlinear evolution of the Buneman instability driven by an external electric field by particle-in-cell (PIC) simulations. They observed that the electron solitary waves and ion acoustic waves were excited and a broad electron velocity distribution function (EVDF) plateau formed at the final stage of the instability. However, the dimension of their simulations was relatively narrow with only 128 Debye lengths, and the simulations were run for only 2000 electron plasma periods. The small system length and simulation time hinder the observation of the large-scale structures and long-term effects. Therefore, in this paper, we conducted a prolonged simulation (up to 3.5×10^5 electron plasma periods) with a larger system length (1000 Debye lengths). In addition to the electron phase-space holes, the formation of ion phase-space holes and the intermittent nature of turbulence are also observed in our simulations, providing new insights into the nonlinear processes of turbulence in current-carrying plasmas.

The paper is organized as follows: the PIC model and its benchmark with linear dispersion relation are presented in Sec. II. Simulation results are discussed in Sec. III, and a summary is provided in Sec. IV.

II. NUMERICAL MODEL

A. Model descriptions

In this paper, a one-dimensional calculation domain is adopted to simulate the current-driven instability, as depicted in Fig. 1. Two periodic boundaries are applied at $x = 0$ and $x = L$, i.e., the particles moving out from one side are re-injected on the opposite side. The length of the simulation domain is $L = 1000\lambda_{De}$ (where $\lambda_{De} = \sqrt{\epsilon_0 T_e / en_e} = 6.3 \times 10^{-5}$ m is the electron Debye length for the initial plasma density 10^{17} m^{-3} and electron temperature 7.0 eV, where ϵ_0 is the vacuum permittivity, e is the elementary charge, T_e is the electron temperature, and n_e is the electron number density), upon which a constant electric field $E_0 = 5.0 \text{ V/m}$ is imposed to maintain the current. We also perform

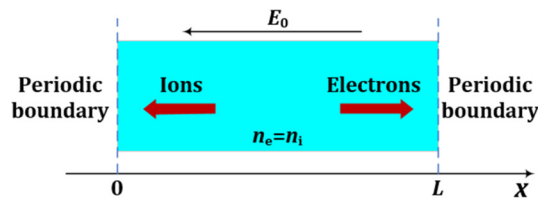


FIG. 1. Schematic diagram of the one-dimensional simulation domain. It includes a homogeneous plasma with equal electron and ion number density, i.e., $n_e = n_i = 10^{17} \text{ m}^{-3}$. A constant electric field $E_0 = 5.0 \text{ V/m}$ is imposed on the whole domain to maintain the current.

simulation with $L = 2000\lambda_{De}$, and the results demonstrate that the domain size does not affect the physical process. A similar setup was used in Ref. 5, describing an inductive startup of a fusion device. It should be noted that no Buneman instability developed in the simulations of Ref. 5, which may be attributed to the insufficient number of cells (only 32 cells in total were used). Because we only focus on the electrostatic waves propagating parallel to the magnetic field, the magnetic field is neglected in our 1D simulations.

Our simulations start from a homogeneous plasma including the warm ions and electrons with a large relative drift velocity. The mass ratio $m_i/m_e = 1836$, plasma density $n_0 = 10^{17} \text{ m}^{-3}$, electron and ion temperatures are $T_e = T_i = 7.0 \text{ eV}$, and the electron drift velocity $v_{D,0} = 1.56 \times 10^6 \text{ m/s}$ are used as the initial parameters. The thermal velocity is defined as $v_{Te} = \sqrt{2kT_e/m_e}$. Initially, 6.0×10^5 macro-particles are generated for each species. The cell size $\Delta x = 1/3\lambda_{De} = 2.1 \times 10^{-5} \text{ m}$ is chosen to resolve the Debye length (i.e., 3000 cells in total), and the time step $\Delta t = 6.0 \times 10^{-12} \text{ s}$ is selected to resolve the electron plasma frequency ($\omega_e \Delta t = 0.1$ with $\omega_e = \sqrt{e^2 n_e / \epsilon_0 m_e}$ being the plasma electron frequency). The typical simulation time is 12 h utilizing 256 CPU cores.

The simulations in this study are performed using the open-source EDIPIC-1D code. EDIPIC-1D is a parallelized PIC code solving Poisson's equation and particle motion equations based on the direct implicit algorithm²⁶ and can resolve one spatial coordinate and three velocity components (1d3v). It incorporates a model for secondary electron emission, the Monte Carlo model of electron-neutral collisions, and the Langevin model of Coulomb collisions for electrons.²⁷ EDIPIC-1D is equipped with a range of diagnostics to facilitate in-depth analysis of the simulation results. These diagnostics include the capability to extract phase-space data, visualize electron and ion velocity functions, and gather data from electric probes placed within the simulation domain. The EDIPIC-1D code has been successfully applied to simulate the nonlinear wave coupling process.^{28,29} We refer the readers to Ref. 26 for more comprehensive information about the capabilities and methodologies employed in EDIPIC-1D. In the future 2D and 3D simulations can be performed using EDIPIC-2D and LTP-PIC-3D codes.^{30–33}

B. Model verification with linear dispersion relation

To demonstrate the accuracy of the EDIPIC code, we performed a series of simulations of linear dispersion relation. For the initial state, we assume a shifted Maxwellian for electrons and a Maxwellian distribution for ions, namely,

$$f_e = \frac{n_e}{\pi^{1/2} v_{Te}} \exp \left[-\frac{(v - v_D)^2}{v_{Te}^2} \right], \quad f_i = \frac{n_i}{\pi^{1/2} v_{Ti}} \exp \left(-\frac{v^2}{v_{Ti}^2} \right), \quad (1)$$

where v_{Ti} denotes the ion thermal velocity. Correspondingly, the linear dispersion relation of current-driven instability reads

$$1 - \frac{\omega_i^2}{k^2 v_{Ti}^2} Z' \left(\frac{\omega}{kv_{Ti}} \right) - \frac{\omega_e^2}{k^2 v_{Te}^2} Z' \left(\frac{\omega - kv_D}{kv_{Te}} \right) = 0, \quad (2)$$

where ω_i represents the ion plasma frequency. $Z'(\zeta) = \frac{dZ(\zeta)}{d\zeta} = -2(1 + \zeta Z(\zeta))$ is the derivative of $Z(\zeta)$, where $Z(\zeta) = 2i \exp(-\zeta^2) \int_{-\infty}^{\zeta} \exp(-s^2) ds$ is the plasma dispersion function. In the long

wavelength limit, if $|\omega/kv_{Ti}| \gg 1$ and $|(\omega - kv_D)/kv_{Te}| \ll 1$, the dispersion function can be written as

$$\omega_r^2 \approx \frac{k^2 c_s^2}{1 + (k\lambda_{De})^2}, \quad (3)$$

$$\gamma_L \approx \sqrt{\frac{\pi}{8}} \omega_r \left[\frac{\sqrt{2}v_D}{v_{Te}} - \sqrt{\frac{m_e}{m_i}} - \left(\frac{T_e}{T_i}\right)^{3/2} \exp\left(-\frac{T_e}{2T_i}\right) \right],$$

where c_s is the ion-acoustic speed. Thus, the stability threshold for a current-driven plasma is

$$\gamma_L = 0 \Rightarrow \frac{\sqrt{2}v_D}{v_{Te}} - \sqrt{\frac{m_e}{m_i}} - \left(\frac{T_e}{T_i}\right)^{3/2} \exp\left(-\frac{T_e}{2T_i}\right) \approx 0. \quad (4)$$

We performed several test cases to verify the simulation results of EDIPIC against Eq. (4). In these test cases, the mass ratio $m_i/m_e = 1836$ and initial plasma density $n = 10^{17} \text{ m}^{-3}$ are fixed while the ratio v_D/v_{Te} and T_e/T_i are varied. As discussed, a shifted Maxwellian electron distribution function and Maxwellian ion distribution function are adopted initially. The external electric field is removed in all the test cases. The verification of the simulation results against the threshold [Eq. (4)] are plotted in Fig. 2. The black line denotes the threshold and the dots denote the numerical test cases. In particular, the red triangle dots and the blue circular dots represent the cases where the instability does and does not occur. From Fig. 2, one can see that except for several marginal case points, all the other numerical case points correspond to the stability regimes as predicted by Eq. (4), indicating that the EDIPIC simulation results show a good agreement with the linear dispersion relation. The stability boundary given by linear theory was reproduced successfully, which provides a basis for applying our model to investigate the evolution of current-driven instability.

III. RESULTS AND DISCUSSION

Figures 3(a) and 3(b) present the time evolutions of the instantaneous electron drift velocity v_D and the thermal velocity $v_{Te||}$, the

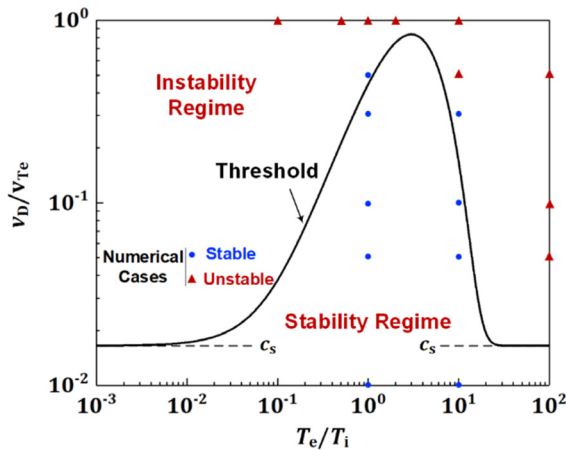


FIG. 2. Verification of EDIPIC simulations results against Eq. (4) with v_D/v_{Te} and T_e/T_i varied. For all the cases in this figure, the external electric field is removed. The black line is the stability threshold [Eq. (4)], and the dots represent the numerical test cases: the red triangle dots and the blue circular dots denote the cases where the instability does and does not occur, respectively.

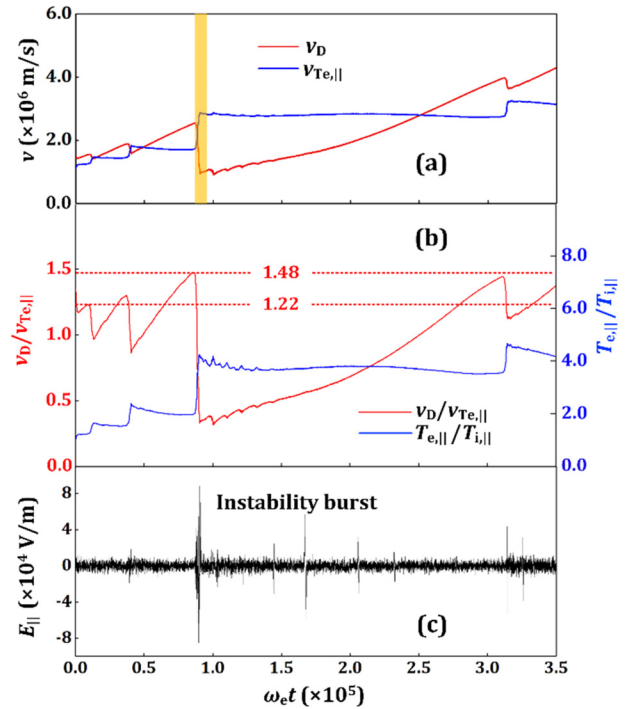


FIG. 3. Evolution of (a) the electron drift velocity v_D (averaged over the entire domain) and the thermal velocity $v_{Te||}$, (b) the velocity ratio $v_D/v_{Te||}$ and the temperature ratio $T_{e||}/T_{i||}$, and (c) the electric field $E_{||}$ at $x = 158\lambda_{De}$. The simulation parameters are $m_i/m_e = 1836$, $n = 10^{17} \text{ m}^{-3}$, $T_e = T_i = 7.0 \text{ eV}$, and $v_D = 1.56 \times 10^6 \text{ m/s}$.

velocity ratio $v_D/v_{Te||}$ and the temperature ratio $T_{e||}/T_{i||}$, respectively. To capture the temporal evolutions of the instability, a probe is placed at $x = 158\lambda_{De}$ to record the instantaneous intensity of the electric field $E_{||}(t)$ from $\omega_e t = 0$ to 3.5×10^5 , as depicted in Fig. 3(c). Here, $T_{e||}$ and $T_{i||}$ are defined as $T_{e||} = m_e(\langle v_{e||}^2 \rangle - \langle v_{e||} \rangle^2)$ and $T_{i||} = m_i(\langle v_{i||}^2 \rangle - \langle v_{i||} \rangle^2)$, where $v_{e||}$ and $v_{i||}$ are the parallel component of the particle velocity vector for the respective species, and $\langle \cdot \rangle$ denotes the averages over all the macro-particles of each species.

As shown in Fig. 3(a), the time evolutions of v_D and $v_{Te||}$ show a quasiperiodic pattern. In each period, v_D increases at first due to the acceleration of electrons by the external electric field. When the ratio of $v_D/v_{Te||}$ reaches the threshold (in the range 1.22–1.48), the Buneman instability quickly develops by generating bursts of strong electric fields; this strong wave electric field decelerates the electron drift [see Figs. 3(b) and 3(c)] followed by rapid electron heating, leading to the decrease in v_D and the increase in $v_{Te||}$. The ratio of $v_D/v_{Te||}$ then falls below the threshold, and thus, the instability decays until electrons are accelerated to reach and cross the instability threshold once again. As shown in Fig. 3(b), the interval between two peaks of $v_D/v_{Te||}$ increases. This increase in time between peaks is likely attributed to the following two reasons: (i) The temperature ratio, $T_{e||}/T_{i||}$, is rising, which raises the threshold of $v_D/v_{Te||}$ required to generate Buneman instability. Consequently, electrons need more acceleration time to cross this threshold; (ii) following the burst, the waves undergo gradual damping. This signifies that a period of time is needed for the system to settle down, and the stronger the preceding burst, the longer

this period persists, and the stronger the previous burst, the longer this period lasts. Throughout this duration, electrons can still experience deceleration by the waves, thus requiring more time to cross the threshold. As depicted in Fig. 3(c), the electric field $E_{||}$ exhibits pulses of spike fluctuations, corresponding to the instability burst and decay, indicating the intermittent nature of the turbulence, consistent with the recent MMS observations.^{10,24}

Figure 4(a) zooms in on the evolution of v_D and $v_{Te,||}$ within the time window $\omega_e t = 84\,000$ – $92\,000$. One can see that during the burst phase, electrons experience two stages of heating. We abbreviate them as SHS (slow heating stage) and FHS (fast heating stage), respectively. SHS, the first stage, lasts for approximately 1000 electron plasma periods. Later on, the FHS starts when the maximum heating rate becomes much higher. The heating of electrons correlates with the variations of electron velocity distribution functions (EVDFs). As depicted in Fig. 4(b), from $\omega_e t = 87\,256$ to $\omega_e t = 88\,110$ at SHS (see red and dark blue curves), only slow electrons (referred to the electrons with velocity below $v_{Te,||}$) are affected. However, from $\omega_e t = 88\,110$ to $\omega_e t = 90\,690$ at the FHS stage (see dark blue and yellow curves), the pronounced peak of EVDF at $v_{e,||} = 3v_{Te,||}$ has been flattened, indicating that most of the drift electrons are thermalized. Ultimately, a big plateau with the width of $\sim 5v_{Te,||}$ is created. We will show that the plateau formation is not due to the well-known quasi-linear diffusion, but instead, the different variations of EVDF at SHS and FHS are caused by corresponding nonlinear processes that will be discussed hereafter.

Figures 5(a)–5(c) display the space–time evolution of the electric field during the time interval $\omega_e t = 86\,330$ – $90\,327$. We also perform the 2D fast Fourier transform (FFT) of the electric field and plot the resulting energy spectra $|E_{||}(k, \omega)|^2$ in Figs. 5(d)–5(f), respectively. At $\omega_e t = 86\,330$ – $87\,220$, the velocity threshold has not yet been attained. The amplitude of electric field fluctuations remains small. As shown in Fig. 5(d), three branches of waves are observed, of which two have low phase velocity ($v_{ph} = \omega_r/k$). Their real frequency ω_r and the wave number k follow the dispersion relation of the ion acoustic wave. Note that we call them ion acoustic solitary waves (IASWs) because they have a solitary structure.

The third branch also exhibits an acoustic-type dispersion with a phase velocity of 1.1×10^6 m/s. This value is much higher than the ion acoustic speed $c_s = 2.8 \times 10^4$ m/s. We interpret these modes as the nonlinear *electron acoustic solitary waves* (EASWs) for the following three reasons (similar to the findings of Refs. 34–37): (i) The EVDF has the trapped electron population near the phase velocity of EASWs, which makes EASWs not suffer the Landau damping; (ii) the waves

have solitary packet structure; and (iii) the value of the wave phase velocity satisfies the dispersion relation calculated for an EVDF with a plateau (see the Appendix). Bursts of electron-acoustic solitary waves after IASWs are also observed in a recent study.³⁸

After $\omega_e t = 87\,220$, the instability burst occurs and it comes to the SHS, where the energy density of the EASWs rises by three orders of magnitude, as depicted in Fig. 5(e). Correspondingly, several coherent large-amplitude wave packets are observed in Fig. 5(b). These wave packets emanate from an IASW packet and propagate along the electron drift direction with a speed aligned with the phase velocity of EASWs ($\sim 1.1 \times 10^6$ m/s). The ejection of EASW packets emanating from the IASW also signifies an unforeseen coupling between the relatively slow ion dynamics and the fast electron dynamics. The exact details of the process will require special follow-up studies.

After $\omega_e t = 88\,110$, at FHS, one can see from Fig. 5(f) that only the ion acoustic waves are seen, which have the phase speed of several ion acoustic speeds. As depicted in Fig. 5(c), the coherent EASW packets disappear, and instead, a turbulent state emerges. Particles can still experience deceleration by the turbulence, causing the slower rise of $v_D/v_{Te,||}$ [see Fig. 3(b)].

Figure 6 presents the potential profiles at various time points at the burst stage. As shown in Fig. 6(a), at the beginning of the instability burst ($\omega_e t = 87\,256$), a wave packet with the amplitude of 10 V occurs near the left boundary. This wave packet moves with a speed closely aligned with the ion acoustic speed, indicating that it is the IASW packet. Subsequently at the SHS ($\omega_e t = 87\,747$), the EASW packet, characterized as a potential hump, has formed. Except for the pronounced EASW packet, the amplitude of the potential fluctuations is small. In contrast, at FHS ($\omega_e t = 90\,158$), the potential profile exhibits large fluctuations over the whole simulation domain. In addition, a spiky potential well is observed, which corresponds to the formation of ion holes in phase space.

The snapshots of the electron phase space [Figs. 7(a1)–7(e1)] and the ion phase space [Figs. 7(a2)–7(e2)] are plotted to highlight the mechanism of electron heating and plateau formation. For clarity, in this paper, we follow the definition from Ref. 39, and apply the term “electron-hole” (and “ion hole”) to a localized region where the electron (and ion) density is lower because of the reduced phase-space density on trapped particle orbits. Furthermore, for better clarification, if the electrons are trapped in an IASW (or EASW) potential and create an electron-hole as a result, we call it “IASW-EH” (or “EASW-EH”).

Instead of the quasi-linear diffusion in velocity space, Fig. 7 clearly shows the occurrence of complex nonlinear processes in phase space. As

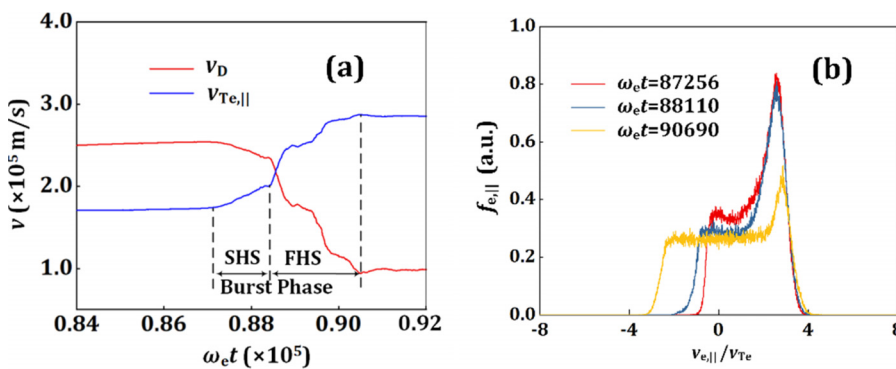


FIG. 4. (a) Zoom-in view of the evolution of the electron drift velocity, v_D , and the thermal velocity $v_{Te,||}$ during the burst phase [the orange zoom-in window in Fig. 3(a)], where SHS and FHS represent the slow and fast electron heating stages, respectively. (b) Electron velocity distribution functions at different time points. The simulation parameters are $m/m_e = 1836$, $n = 10^{17} \text{ m}^{-3}$, $T_e = T_i = 7.0 \text{ eV}$, and $v_D = 1.56 \times 10^6 \text{ m/s}$.

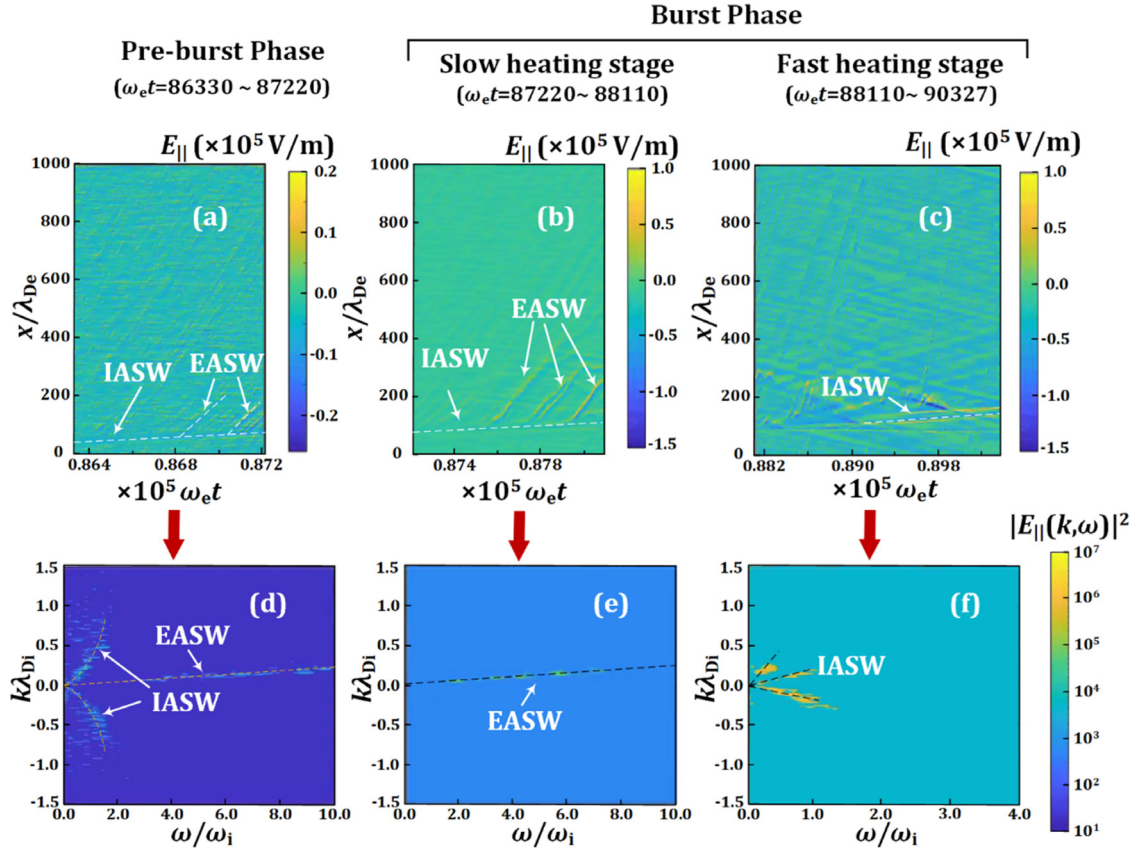


FIG. 5. Evolution of the wave energy density and the electric field fluctuations. (a)–(c) Fluctuations of $E_{||}$ (x, t) and (d)–(f) wave energy spectrum $|E_{||}(k, \omega)|^2$ at the pre-burst phase ($\omega_e t = 86\,330$ – $87\,220$), the slow-heating stage ($\omega_e t = 87\,220$ – $88\,110$) and the fast-heating stage ($\omega_e t = 88\,110$ – $90\,327$). λ_{De} is the ion Debye length. “IASW” and “EASW” denote the ion- and electron acoustic solitary waves, respectively.

depicted in Fig. 7(a1), at the very beginning of the SHS ($\omega_e t = 87\,256$), an electron-hole (EH) forms at $x = 90\lambda_{De}$, which is due to the electron trapping in the IASW packet [see Fig. 7(a1)]. The IASW packet is generated by the Buneman instability that occurs when the ratio of $v_D/v_{Te,||}$ reaches the threshold. Electrons with the velocity below $v_{Te,||}$ will be trapped in the potential structure of the IASW packet, thereby forming the IASW-EH. This IASW-EH is a slow electron-hole

propagating with the speed $\sim c_s$, depleting the local ions [see Fig. 7(a2)]. The excitation of this IASW-EH modifies the local EVDFs, thereby supporting the growth of EASWs. As shown in Fig. 7(b1), at SHS, electrons are trapped in the EASW packet, creating the EASW-EHs. Therefore, they are slowed down and thermalized in EASW-EHs, creating a plateau in the vicinity of $v = v_{Te,||}$, as depicted in Fig. 4(b). Namely, the interaction of electrons and EASWs plays a primary role

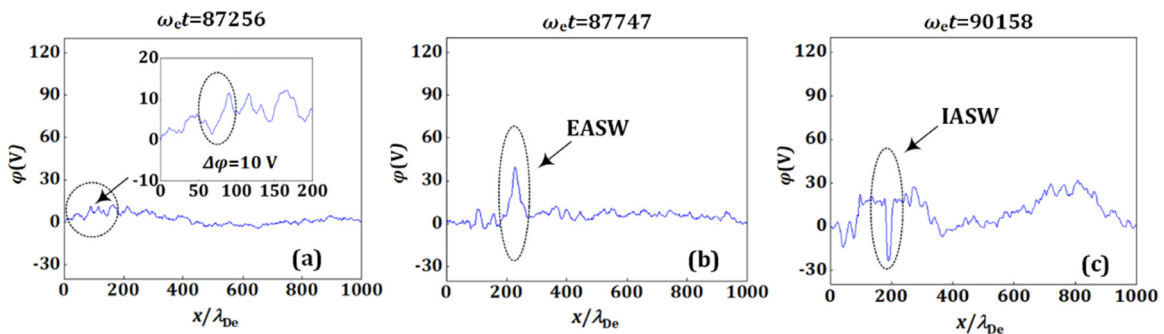


FIG. 6. Potential profiles at various times: (a) $\omega_e t = 87\,256$; (b) $\omega_e t = 87\,747$; and (c) $\omega_e t = 90\,158$.

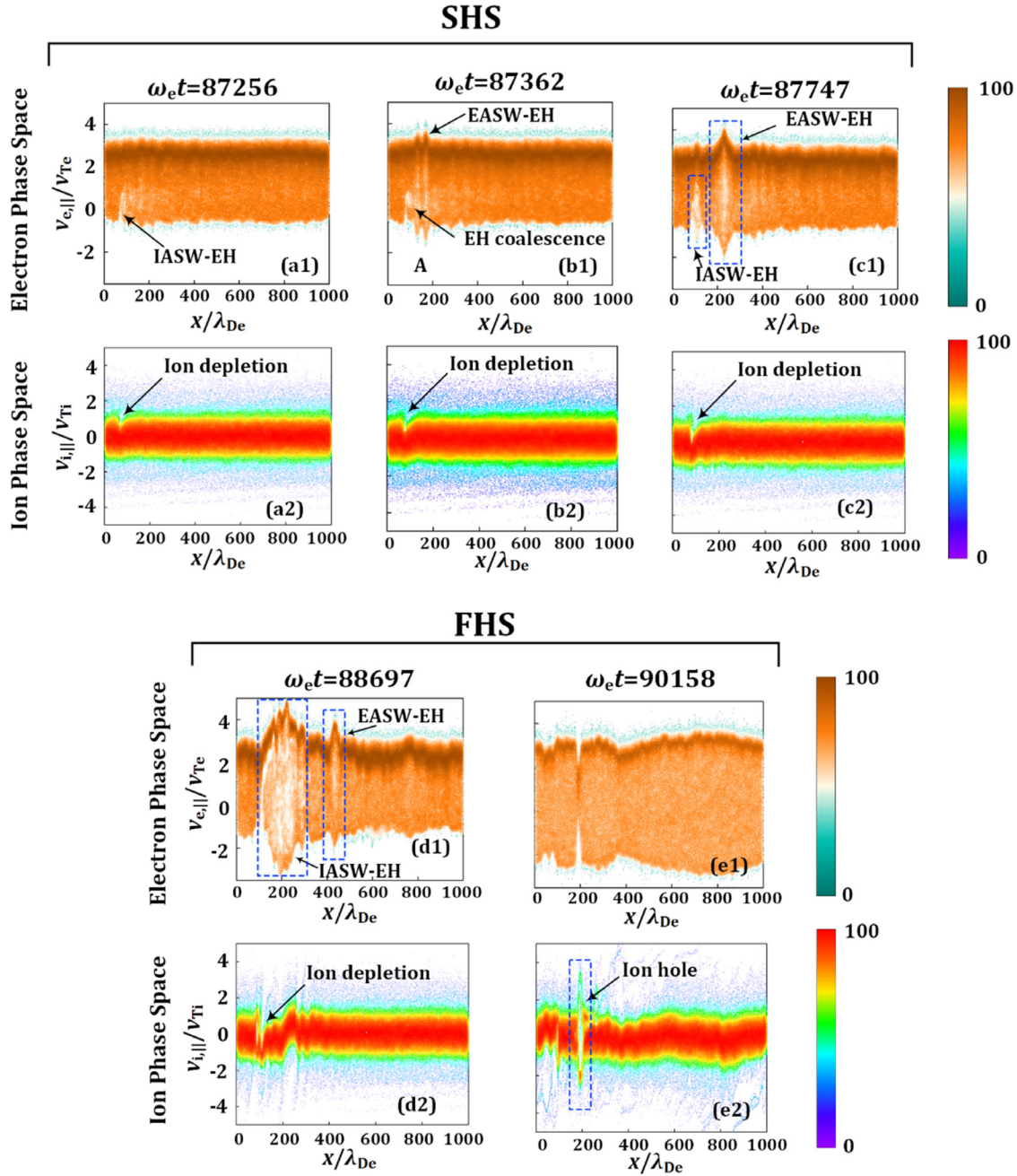


FIG. 7. The snapshots of the electron phase space, the ion phase space, and the profiles of the electrical potential. The letters “a” to “e” correspond to different moments in time evolution, and the numbers “1” and “2” refer to the electron phase space and the ion phase space, respectively. “EH” denotes the “electron-hole” formed due to the trapping of electrons by the large-amplitude waves. EASW-EH and IASW-EH denote the “electron-hole” formed due to the trapping of electrons by EASWs and IASWs.

in electron heating and plateau formation at SHS. The variations of EVDF at the SHS are sketched in Figs. 8(a) and 8(b).

As stated above, the amplitude of the potential well of the IASW packet is around 10 V at the very beginning of the burst stage. Therefore, only the slow electrons with velocity below $v_{Te||}$ can be trapped in IASW-EH. However, since EASW-EHs create many

decelerated electrons (and these electrons are released after the decay of EASW-EHs), the IASW-EH can further trap more slow electrons, thus supporting the growth of IASW-EH. The growth of IASW-EH can be seen in Figs. 7(b1) and 7(c1). Ultimately, a giant IASW-EH forms at $\omega_e t = 88697$ at FHS. As shown in Fig. 7(d1), this IASW-EH traps the electrons at the velocity up to $3v_{Te||}$. In this IASW-EH, a

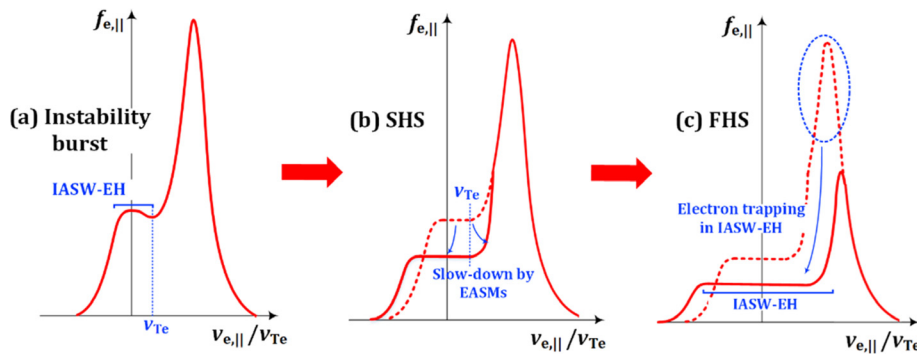


FIG. 8. Schematics of the variations of EVDF manifesting the electron heating at SHS and FHS. The solid lines represent the EVDF at the present stage and the dotted lines represent the EVDF from the previous stage.

strong phase mixing allows a rapid energy exchange between the high- and low-energy electron population. As a result, rapid electron heating is produced at FHS and a huge plateau is created. Namely, at FHS, electron heating and plateau formation are attributed to the complex nonlinear interaction between IASW and EASW. The variation of EVDF at the FHS is sketched in Fig. 8(c).

For ions, they are rarely affected by EASWs in phase space because they are too slow to be resonant with EASWs, as shown in Figs. 7(a2)–7(c2). Only the ions at $x = 90\lambda_{De}$ are depleted by the potential of the IASW packet. The depletion becomes stronger with the growth of IASW-EH [Fig. 7(d2)]. At $\omega_e t = 90158$, the giant IASW-EH breaks. Correspondingly, an ion hole is formed. The ion hole was not seen in previous simulations, e.g., the study of Omura *et al.*,²⁵ because both their system length and the simulation time are too small to capture the formation of giant IASW-EH.

IV. CONCLUSIONS

In this paper, we study the evolution of turbulence ignited by an external electric field in current-carrying plasmas by performing a long-term particle-in-cell simulation. The primary findings are summarized as follows:

- (1) We unveil the intermittent nature of the current-driven instability. Once $v_D/v_{Te,||}$ crosses the threshold 1.22–1.48, the instability initiates a burst phase, during which v_D falls while $v_{Te,||}$ rises rapidly, ultimately causing the $v_D/v_{Te,||}$ ratio to drop below the threshold. Consequently, the instability subsides until the electrons are accelerated and $v_D/v_{Te,||}$ crosses the threshold once again.
- (2) We identify that the electron heating and the formation of plateau of EVDF are not due to the quasi-linear diffusion in velocity space but the complex interaction between ion- and electron-acoustic solitary waves.
- (3) In addition to the EHs, we also observe the formation of an ion phase-space hole. The missing of ion hole in previous simulations may be attributed to the insufficient system length and simulation time.

SUPPLEMENTARY MATERIAL

See the supplementary material for video illustrating the evolution of the potential, number density, electron, and ion phase space between $\omega_e t = 85019$ and $\omega_e t = 94020$. The selected time window covers one burst period.

ACKNOWLEDGMENTS

The work of Jian Chen and He-Ping Li was supported by the China Scholarship Council and the National Natural Science Foundation of China under Grant Nos. 11775128 and 12305223. The work of Alexander V. Khrabrov and Igor D. Kaganovich was supported by the Princeton Collaborative Research Facility (PCRF) and Laboratory Directed Research & Development (LDRD) projects, which are funded by the U.S. Department of Energy (DOE) under Contract No. DE-AC02-09CH11466. The authors are very grateful to Haomin Sun, Dr. Liang Xu, and Dr. Sarveshwar Sharma for fruitful discussions. The authors thank the referees for the careful reading and really helpful comments in improving this manuscript.

AUTHOR DECLARATIONS

Conflict of Interest

The authors have no conflicts to disclose.

Author Contributions

Jian Chen: Conceptualization (equal); Data curation (lead); Formal analysis (lead); Writing – original draft (lead). **Alexander V. Khrabrov:** Investigation (equal); Methodology (equal); Writing – review & editing (equal). **Igor D. Kaganovich:** Conceptualization (lead); Funding acquisition (equal); Supervision (equal); Writing – original draft (equal); Writing – review & editing (equal). **He-Ping Li:** Funding acquisition (equal); Supervision (equal); Writing – review & editing (equal).

DATA AVAILABILITY

The data that support the findings of this study are available from the corresponding authors upon reasonable request.

APPENDIX: PLATEAU EVDF SUPPORTING EASWS

In this appendix, we will show that the presence of EASWs can be supported by the formation of the plateau EVDF. At the pre-burst phase and the very beginning of the burst phase, the EVDF can be approximated using a shifted Maxwellian distribution function (for the drift electrons) plus a plateau distribution function (for the trapped electrons) [see Fig. 4(b)]. The plateau width is $\sim v_{Te}$,

and it covers the velocity range from $v \approx 0$ to $v \approx v_{Te}$. The drift velocity of the drift electron population becomes $v_D \approx 2.4 v_{Te}$. Since the plateau is small, the drift population is not strongly affected and can be written as

$$f_{e,drift} = C \exp \left[-\frac{(v - v_D)^2}{v_{Te}^2} \right], \quad v \geq v_{Te}, \quad (A1)$$

where C is a constant parameter to maintain the number density. The trapped population can be approximated by

$$f_{e,Trapped} = C \exp \left[-\frac{(v_{Te} - v_D)^2}{v_{Te}^2} \right], \quad 0 \leq v < v_{Te}, \quad (A2)$$

where $f_{e,Trapped} = f_{e,drift}(v_{Te})$ is used. Therefore, the complete EVDF can be written as

$$f_e = \begin{cases} C \exp \left[-\frac{(v - v_D)^2}{v_{Te}^2} \right], & v \geq v_{Te}, \\ 0, & v < 0, \\ C \exp \left[-\frac{(v_{Te} - v_D)^2}{v_{Te}^2} \right], & 0 \leq v < v_{Te}. \end{cases} \quad (A3)$$

We only deal with the weak EASWs and the electron density perturbation is small. Therefore, the integral of EVDF over velocity should be equal to n_e . It gives $C = 0.97 n_e / (\pi^{1/2} v_{Te}) \approx n_e / (\pi^{1/2} v_{Te})$.

We then follow the treatment in Ref. 35 to calculate the phase velocity of EASWs, $v_{ph,EASW}$. At first, we can shift the EVDF to the EASW frame, and thus, the EVDF reads

$$f_e = \begin{cases} \frac{n_e}{\sqrt{\pi} v_{Te}} \exp \left[-\frac{(v - v_D + v_{ph,EASW})^2}{v_{Te}^2} \right], & v \geq (v_{Te} - v_{ph,EASW}), \\ 0, & v < -v_{ph,EASW}, \\ \frac{n_e}{\sqrt{\pi} v_{Te}} \exp \left[-\frac{(v_{Te} - v_D + v_{ph,EASW})^2}{v_{Te}^2} \right], & -v_{ph,EASW} \leq v < (v_{Te} - v_{ph,EASW}). \end{cases} \quad (A4)$$

Since the EASWs are fast, they hardly perturb the ions. Thus, for ions, the ion distribution function (IVDF) in the EASW frame can be written as

$$f_i = \frac{n_i}{\sqrt{\pi} v_{Ti}} \exp \left[-\frac{(v + v_{ph,EASW})^2}{v_{Ti}^2} \right]. \quad (A5)$$

In Ref. 35, the dispersion relation for EASWs with plateau distribution function reads

$$k^2 = \frac{4\pi e^2}{m_e} \int_{-\infty}^{\infty} \frac{1}{v} \frac{\partial F_e}{\partial v} dv + \frac{4\pi e^2}{m_i} \int_{-\infty}^{\infty} \frac{1}{v} \frac{\partial F_i}{\partial v} dv, \quad (A6)$$

where $F_e = 1/2 [f_e(v) + f_e(-v)]$ and $F_i = 1/2 [f_i(v) + f_i(-v)]$ are the even part of EVDF, and e is the unit charge. Substituting Eqs. (A4) and (A5) into Eq. (A6), we have

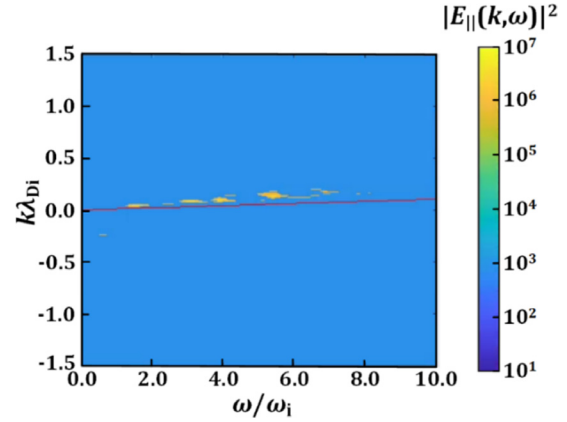


FIG. 9. EASW spectrum predicted by Eq. (A7) against the spectrum from simulation. The color plot denotes the Fast Fourier Transform spectrum of the electric field extracted from the simulation and the red line denotes the spectrum predicted by Eq. (A7).

$$k^2 = \frac{2\omega_e^2}{\sqrt{\pi} v_{Te}^3} \int_{v_{Te}-v_{ph,EASW}}^{\infty} \left\{ \frac{v_D - v_{ph,EASW} - v}{v} \times \exp \left[-\left(\frac{v_D - v_{ph,EASW} - v}{v_{Te}} \right)^2 \right] - \frac{v_D - v_{ph,EASW} + v}{v} \times \exp \left[-\left(\frac{v_D - v_{ph,EASW} + v}{v_{Te}} \right)^2 \right] \right\} dv \\ + \frac{2\omega_i^2}{\sqrt{\pi} v_{Ti}^3} \int_{-\infty}^{\infty} \left\{ \frac{v_{ph,EASW} + v}{v} \times \exp \left[-\left(\frac{v_{ph,EASW} + v}{v_{Ti}} \right)^2 \right] + \frac{v - v_{ph,EASW}}{v} \times \exp \left[-\left(\frac{v - v_{ph,EASW}}{v_{Ti}} \right)^2 \right] \right\} dv. \quad (A7)$$

Here, we look for the phase velocity of EASWs, which is of the order of electron thermal velocity. The EASW spectra predicted by Eq. (A7) are then plotted against the FFT spectrum from the simulation in Fig. 9. As shown, a good agreement is achieved, demonstrating that the EASWs can be supported by the plateau electron distribution function.

REFERENCES

- ¹A. A. Galeev and R. Z. Sagdeev, in *Review of Plasma Physics*, edited by M. A. Leontovich (Plenum, New York, 1979), Vol. 6, p. 141.
- ²A. L. Ortega, B. A. Jorns, and I. G. Mikellides, *J. Propul. Power* **34**, 1026–1038 (2018).
- ³A. Smolyakov, T. Zintel, L. Couedel, D. Sydorenko, A. Umnov, E. Sorokina, and N. Marusov, *Plasma Phys. Rep.* **46**, 496–505 (2020).
- ⁴B. A. Jorns, I. G. Mikellides, D. M. Goebel, and R. Wirz, *Phys. Rev. E* **96**, 023208 (2017).
- ⁵W. Jiang, Y.-L. Peng, Y. Zhang, and G. Lapenta, *Nucl. Fusion* **56**, 126017 (2016).
- ⁶H. De Kluiver, C. J. Barth, and A. J. H. Donne, *Plasma Phys. Controlled Fusion* **30**, 699–719 (1988).
- ⁷K. Hara and C. Treece, *Plasma Sources Sci. Technol.* **28**, 055013 (2019).

- ⁸M. P. Georjgin and M. S. McDonald, *J. Appl. Phys.* **130**, 243306 (2021).
- ⁹Y. V. Khotyaintsev, A. Vaivads, M. André, M. Fujimoto, A. Retinò, and C. J. Owen, *Phys. Rev. Lett.* **105**, 165002 (2010).
- ¹⁰Y. V. Khotyaintsev, D. B. Graham, K. Steinvall, L. Alm, A. Vaivads, A. Johlander, C. Norgren, W. Li, A. Divin, H. S. Fu *et al.*, *Phys. Rev. Lett.* **124**, 045101 (2020).
- ¹¹H. Che, J. F. Drake, M. Swisdak, and P. H. Yoon, *Phys. Rev. Lett.* **102**, 145004 (2009).
- ¹²L. Andersson, R. E. Ergun, J. Tao, A. Roux, O. LeContel, V. Angelopoulos, J. Bonnell, J. P. McFadden, D. E. Larson, S. Eriksson *et al.*, *Phys. Rev. Lett.* **102**, 225004 (2009).
- ¹³D. L. Newman, M. V. Goldman, R. E. Ergun, and A. Mangency, *Phys. Rev. Lett.* **87**, 255001 (2001).
- ¹⁴O. Buneman, *Phys. Rev.* **115**, 503 (1959).
- ¹⁵P. H. Yoon, *Phys. Plasmas* **25**, 011603 (2018).
- ¹⁶P. H. Yoon, *Phys. Plasmas* **7**, 4858 (2000).
- ¹⁷A. Tavassoli, M. Shoucri, A. Smolyakov, M. P. Zadeh, and R. J. Spiteri, *Phys. Plasmas* **28**, 022307 (2021).
- ¹⁸J. Pavan, P. H. Yoon, and T. Umeda, *Phys. Plasmas* **18**, 042307 (2011).
- ¹⁹P. H. Yoon, *Phys. Phys. Plasmas* **17**, 112316 (2010).
- ²⁰P. H. Yoon and T. Umeda, *Phys. Plasmas* **17**, 112317 (2010).
- ²¹P. A. Muñoz and J. Büchner, *Phys. Rev. E* **98**, 043205 (2018).
- ²²Y. V. Khotyaintsev, D. B. Graham, C. Norgren, and A. Vaivads, *Front. Astron. Space Sci.* **6**, 70 (2019).
- ²³A. R. Vazsonyi, K. Hara, and I. D. Boyd, *Phys. Plasmas* **27**, 112303 (2020).
- ²⁴C. Norgren, D. B. Graham, M. R. Argall, K. Steinvall, M. Hesse, Y. V. Khotyaintsev, A. Vaivads, P. Tenfjord, D. J. Gershman, P.-A. Lindqvist *et al.*, *Phys. Plasmas* **29**, 012309 (2022).
- ²⁵Y. Omura, W. J. Heikkilä, T. Umeda, K. Ninomiya, and H. Matsumoto, *J. Geophys. Res.* **108**, 1197, <https://doi.org/10.1029/2002JA009573> (2003).
- ²⁶D. Sydorenko, Ph.D. thesis, University of Saskatchewan, 2006.
- ²⁷B.-M. Jin, J. Chen, A. V. Khrabrov, Z.-B. Wang, and L. Xu, *Plasma Sources Sci. Technol.* **31**, 115015 (2022).
- ²⁸D. Sydorenko, I. D. Kaganovich, P. L. G. Ventzek, and L. Chen, *Phys. Plasmas* **25**, 011606 (2018).
- ²⁹L. Xu, A. Smolyakov, S. Janhunen, and I. Kaganovich, *Phys. Plasmas* **27**, 080702 (2020).
- ³⁰Q.-C. Cao, J. Chen, H.-M. Sun, G.-Y. Sun, S.-G. Liu, C. Tan, and Z.-B. Wang, *Phys. Plasmas* **30**, 103501 (2023).
- ³¹H.-M. Sun, S. Banerjee, S. Sharma, A. T. Powis, A. V. Khrabrov, D. Sydorenko, J. Chen, and I. D. Kaganovich, *Phys. Plasmas* **30**, 103509 (2023).
- ³²A. T. Powis, J. A. Carlsson, I. D. Kaganovich, Y. Raites, and A. Smolyakov, *Phys. Plasmas* **25**, 072110 (2018).
- ³³S. Rauf, D. Sydorenko, S. Jubin, W. Villafana, S. Ethier, A. Khrabrov, and I. Kaganovich, *Plasma Sources Sci. Technol.* **32**, 055009 (2023).
- ³⁴R. Pottelette, R. E. Ergun, R. A. Treumann, M. Berthomier, C. W. Carlson, J. P. McFadden, and I. Roth, *Geophys. Res. Lett.* **26**, 2629, <https://doi.org/10.1029/1999GL900462> (1999).
- ³⁵J. P. Holloway and J. J. Dornring, *Phys. Rev. A* **44**, 3856 (1991).
- ³⁶F. Valentini, T. M. O'Neil, and D. H. Dubin, *Phys. Plasmas* **13**, 052303 (2006).
- ³⁷F. Anderegg, C. F. Driscoll, D. H. Dubin, T. M. O'Neil, and F. Valentini, *Phys. Plasmas* **16**, 055705 (2009).
- ³⁸Z. Liu, R. White, L. M. Milanese, and N. F. Loureiro, *J. Plasma Phys.* **90**, 965900101 (2024).
- ³⁹I. H. Hutchinson, *Phys. Plasmas* **24**, 055601 (2017).